

Radiance backscattered by a strongly scattering medium in the high spatial frequency limit

BOAZ ILAN,¹ ARNOLD D. KIM,^{1,*}  AND VASAN VENUGOPALAN² 

¹Department of Applied Mathematics, University of California, Merced, 5200 North Lake Road, Merced, California 95343, USA

²Department of Chemical and Biomolecular Engineering, University of California, Irvine, Irvine, California 92697, USA

*Corresponding author: adkim@ucmerced.edu

Received 2 May 2022; revised 19 May 2022; accepted 19 May 2022; posted 20 May 2022; published 13 June 2022

We study the radiative transfer of a spatially modulated plane wave incident on a half-space composed of a uniformly scattering and absorbing medium. For spatial frequencies that are large compared to the scattering coefficient, we find that first-order scattering governs the leading behavior of the radiance backscattered by the medium. The first-order scattering approximation reveals a specific curve on the backscattered hemisphere where the radiance is concentrated. Along this curve, the radiance assumes a particularly simple expression that is directly proportional to the phase function. These results are inherent to the radiative transfer equation at large spatial frequency and do not have a strong dependence on any particular optical property. Consequently, these results provide the means by which spatial frequency domain imaging technologies can directly measure the phase function of a sample. Numerical simulations using the discrete ordinate method along with the source integration interpolation method validate these theoretical findings. © 2022 Optica Publishing Group

<https://doi.org/10.1364/JOSAA.462683>

1. INTRODUCTION

The emergence and development of spatial frequency domain imaging (SFDI) over the past 15 years has made a powerful tool for wide-field imaging of functional and morphological properties of biological tissues broadly available [1–3]. SFDI's use of illumination at multiple spatial frequencies enables the interrogation of turbid samples with varying depth sensitivity and access to structural and compositional information over mesoscopic and macroscopic scales [4,5]. Soon after the emergence of SFDI, investigators began to examine the use of high spatial frequencies to probe the structural morphology of superficial tissues [6,7]. It was understood intuitively that illumination using high spatial frequencies is related to probing tissues using short source-detector separations [8,9], thereby providing sensitivity to metrics related to the angular distribution of single scattering [10]. This notion has been used to extract morphological biomarkers suitable for discrimination between tissue types [6,7,11]. Thus the use of high-frequency illumination with SFDI, coupled with angularly resolved detection, may represent an alternate experimental approach to goniometry [12], angle-resolved low coherence interferometry [13–15], and angular domain scattering interferometric microscopy [16] as a means of providing detailed morphological characterization of samples.

SFDI represents a measurement taken in the spatial Fourier domain. Coincidentally, Fourier transform methods have been used extensively to study three-dimensional radiative transfer. Typically, Fourier transform methods are used for

problems with planar boundaries, e.g., plane-parallel slabs and half-spaces, where Fourier transforms are applied on the coordinates parallel to the planar boundaries. For example, taking the Fourier transform of the radiative transfer equation (RTE) is an elementary step in studying the searchlight problem [17–20]. Chang and Ishimaru [21] solve the RTE for beams by Fourier transforming the problem to the spatial frequency domain, solving the transformed problem, and inverse Fourier transforming that solution back to the spatial domain. This approach was used later by Kim and Moscoso within their Chebyshev spectral method for beams [22], and to study beams in forward-peaked scattering media [23]. Fourier transform methods are also used in the method of rotated reference frames to study three-dimensional radiative transfer [24]. Machida [25] has applied this method of rotated reference frames to study SFDI problems. Fourier transform methods also play a fundamental role in the spherical harmonics expansion method utilizing Fourier decomposition (SHEF_N) method of Gardner *et al.* [26]. Using this approach, the transformed problem for a fixed spatial frequency closely relates to the underlying radiative transfer formulation of the SFDI problem.

When solving the RTE in the spatial frequency domain, analysis of the high spatial frequency limit is problematic because the solution oscillates rapidly as a function of depth. Resolving these highly oscillatory solutions becomes a computational challenge because they lead to additional restrictions to the angular resolution, since spatial and angular variables are coupled in radiative transfer. Nevertheless, Chang and Ishimaru

[21] state that “the high-frequency components do not contribute to the final solution of the complete beam wave problem except when the medium has a small equivalent optical thickness.” They then utilize the first-order scattering approximation to obtain the solution at high spatial frequencies.

Although this approach used by Chang and Ishimaru appears to be effective, it is not well known. Moreover, Chang and Ishimaru neither provide a rigorous theoretical framework that justifies the use of the first-order scattering approximation, nor do they define what precisely is meant by a “small equivalent optical thickness.” Here we give an elementary dominant balance argument that justifies the first-order scattering approximation for high spatial frequencies and give a precise meaning for the small equivalent optical thickness described by Chang and Ishimaru.

The first-order scattering approximation reveals the backscattered radiance to be proportional to the phase function on the backscattered hemisphere. Additionally, our analysis of first-order scattering identifies an explicit curve on the backscattered hemisphere where the radiance is highly concentrated. For an index-matched boundary, this curve depends only on the angle of incidence and no other optical properties. The value of the radiance on this curve is proportional to the phase function. For an index-mismatched boundary, this curve is mapped according to Snell’s law, which depends on the relative refractive index. The value of the radiance on this curve is modified by the Fresnel transmission coefficient. This explicit curve provides valuable insight into the specific angular locations where the radiant power of the backscattered light is most concentrated and therefore may inform the design of the configuration of angularly resolved SFDI measurements at high spatial frequencies.

The remainder of this paper is as follows. We discuss the RTE in the spatial frequency domain in Section 2. Using an elementary dominant balance argument, we show that the leading behavior of the backscattered radiance in the high spatial frequency limit is governed by first-order scattering. In Section 3, we analyze the first-order scattering approximation for the backscattered radiance and identify the curve on which the radiance is concentrated. We show several numerical results in Section 4 that validate this theory. Section 5 contains our conclusions. Appendix A describes the product quadrature rule that we employ in the discrete ordinate method (DOM) used to compute the numerical results in Section 4. Appendix B describes the integration of the source function interpolation method used to compute the numerical results in Section 4.

2. RADIATIVE TRANSFER IN THE SPATIAL FREQUENCY DOMAIN

Consider a plane wave that is spatially modulated along the x direction with spatial frequency f_x incident on the half-space $z > 0$ in direction $\hat{\mathbf{s}}_0$, a vector on the xz plane. The half-space is composed of a uniform absorbing and scattering medium with absorption coefficient μ_a and scattering coefficient μ_s . The radiance L gives the power flowing in direction $\hat{\mathbf{s}}$ at position \mathbf{r} . For this problem, L satisfies the following boundary value problem for the RTE,

$$\hat{\mathbf{s}} \cdot \nabla L + \mu_a L + \mu_s L = \mu_s \int_{4\pi} p(\hat{\mathbf{s}} \cdot \hat{\mathbf{s}}') L(\hat{\mathbf{s}}', \mathbf{r}) d\hat{\mathbf{s}}' \quad \text{in } z > 0, \quad (1a)$$

$$L|_{z=0} = \delta(\hat{\mathbf{s}} - \hat{\mathbf{s}}_0)(L_0 + L_1 \cos(2\pi f_x x + \phi)) + R[L] \quad \text{on } \hat{\mathbf{s}} \cdot \hat{\mathbf{z}} > 0, \quad (1b)$$

with ϕ denoting a spatial phase shift. Here, L_0 and L_1 are the DC and AC components, respectively, of the spatially modulated plane wave. Additionally, we require that $L \rightarrow 0$ as $z \rightarrow +\infty$. The reflection operation, $R[L]$, in Eq. (1b) takes into account any reflections due to a refractive index mismatch on the boundary. In the integral term in Eq. (1a), p denotes the scattering phase function, and integration is taken over the entire unit sphere. We assume that p is spherically symmetric, so $p = p(\hat{\mathbf{s}} \cdot \hat{\mathbf{s}}')$.

In what follows, we study the behavior of L due to L_1 only, and we assume that $L_1 = 1$. In other words, we assume that we can demodulate the DC and AC components of the radiance, which is done effectively in practice (e.g., see [27]). In light of boundary condition [Eq. (1b)], we write $L = \text{Re}[I(\mu, \varphi, z)e^{i(2\pi f_x x + \phi)}]$, where $\mu = \cos \theta$ is the cosine of the polar angle θ and φ is the azimuthal angle. The complex radiance I satisfies the one-dimensional RTE,

$$\mu \partial_z I + \mu_a I = -i2\pi f_x \sqrt{1 - \mu^2} \cos \varphi I - \mu_s \left[I - \int_0^{2\pi} \int_{-1}^1 p(\mu, \mu', \varphi - \varphi') I(\mu', \varphi', z) d\mu' d\varphi' \right], \quad (2a)$$

subject to

$$I(\mu, \varphi, 0) = \delta(\mu - \mu_0)\delta(\varphi) + R[I] \quad \text{on } 0 < \mu \leq 1 \text{ and } 0 \leq \varphi \leq 2\pi, \quad (2b)$$

with incident direction $\mu_0 = \hat{\mathbf{s}}_0 \cdot \hat{\mathbf{z}}$. Additionally, we require that $I \rightarrow 0$ as $z \rightarrow +\infty$. We have written the arguments of p in (2a) to reflect that

$$p(\hat{\mathbf{s}} \cdot \hat{\mathbf{s}}') = p \left[\mu\mu' + \sqrt{(1 - \mu^2)(1 - \mu'^2)} \cos(\varphi - \varphi') \right] = p(\mu, \mu', \varphi - \varphi'). \quad (3)$$

In principle, demodulation methods used to separate DC and AC components of the radiance can also be used to determine the real and imaginary parts of the complex radiance used above [27].

We now utilize the method of dominant balance to study this problem. There are three inverse length scales in Eq. (2a): μ_a , f_x , and μ_s . Let us assume that the medium is strongly scattering, i.e., $\mu_a \ll \mu_s$, and consider the case where μ_a is fixed and is the smallest inverse length scale. It follows that there are two different scaling regimes to consider: $f_x \ll \mu_s$ and $f_x \gg \mu_s$. When $f_x \ll \mu_s$, the leading behavior of I is governed by the diffusion approximation. This result is well understood and has been extensively used to analyze SFDI data acquired at low spatial frequencies [3]. In contrast, when $f_x \gg \mu_s$, we neglect

the term in Eq. (2a) multiplied by μ_s and find that the leading behavior of I satisfies

$$\mu \partial_z I + \mu_a I + i2\pi f_x \sqrt{1 - \mu^2} \cos \varphi I = 0, \quad (4a)$$

subject to

$$I(\mu, \varphi, 0) = \delta(\mu - \mu_0) \delta(\varphi) + R[I] \quad \text{on } 0 < \mu \leq 1 \text{ and } 0 \leq \varphi \leq 2\pi, \quad (4b)$$

from which we determine that, to leading order,

$$I \sim \delta(\mu - \mu_0) \delta(\varphi) \exp\left(-\mu_a z / \mu - i2\pi f_x \sqrt{1 - \mu^2} \cos \varphi z / \mu\right). \quad (5)$$

As $0 < \mu_0 \leq 1$, this result has no contribution on the backscattered hemisphere corresponding to $-1 \leq \mu < 0$. To determine the leading behavior of the backscattered radiance, we use Eq. (2a) and seek a correction \tilde{I} satisfying

$$\begin{aligned} &\mu \partial_z \tilde{I} + \mu_a \tilde{I} + i2\pi f_x \sqrt{1 - \mu^2} \cos \varphi \tilde{I} \\ &= -\mu_s I + \mu_s \int_0^{2\pi} \int_{-1}^1 p(\mu, \mu', \varphi - \varphi') I(\mu', \varphi', z) d\mu' d\varphi', \end{aligned} \quad (6a)$$

subject to

$$\tilde{I}(\mu, \varphi, 0) = R[\tilde{I}] \quad \text{on } 0 < \mu \leq 1 \text{ and } -\pi \leq \varphi \leq \pi. \quad (6b)$$

Substituting Eq. (5) into the right-hand side of Eq. (6a) yields

$$\begin{aligned} &\mu \partial_z \tilde{I} + \mu_a \tilde{I} + i2\pi f_x \sqrt{1 - \mu^2} \cos \varphi \tilde{I} = -\mu_s \delta(\mu - \mu_0) \delta(\varphi) \\ &\quad \times \exp\left(-\mu_a z / \mu - i2\pi f_x \sqrt{1 - \mu^2} \cos \varphi z / \mu\right) \\ &\quad + \mu_s p(\mu, \mu_0, \varphi) \exp\left(-\mu_a z / \mu_0 - i2\pi f_x \sqrt{1 - \mu_0^2} z / \mu_0\right). \end{aligned} \quad (7)$$

This is the governing equation for the first-order scattering approximation. There are two terms in the right-hand side of Eq. (7). The first term only contributes to the forward hemisphere. The second term contributes to both the forward and backward hemispheres. We denote the portions of \tilde{I} on the forward and backward hemispheres by \tilde{I}^+ and \tilde{I}^- , respectively. Solving for \tilde{I}^- using the method discussed by Ishimaru ([28], Section 8-2), we find that

$$\begin{aligned} &\tilde{I}^- = \frac{\mu_s}{2\pi f_x} \\ &\frac{\mu_0 p(\mu, \mu_0, \varphi) \exp\left(-\mu_a z / \mu_0 - i2\pi f_x \sqrt{1 - \mu_0^2} z / \mu_0\right)}{\alpha(\mu_0 - \mu) + i\left(\mu_0 \sqrt{1 - \mu^2} \cos \varphi - \mu \sqrt{1 - \mu_0^2}\right)}, \\ &-1 \leq \mu < 0, \quad 0 \leq \varphi \leq 2\pi, \end{aligned} \quad (8)$$

with $\alpha = \mu_a / (2\pi f_x)$. This result gives the leading behavior of the radiance on the backscattered hemisphere. The reflection

operation $R[I]$ does not come into this calculation until we seek a correction to the radiance on the forward hemisphere.

The first-order scattering approximation is typically applied to problems in optically thin domains or when the albedo is relatively small ([28], Section 8-2). For those problems, first-order scattering can be thought of as a correction to Beer's law [29]. For example, first-order scattering has been applied to the aforementioned searchlight problem [18]. For optically thin domains, Florescu *et al.* [30] have provided an explicit method for solving the inverse problem that uses an extension of the Radon transform. Here, we find that first-order scattering governs the leading behavior of the radiance even though the domain is unbounded and strongly scattering. The analysis given above shows that first-order scattering arises in the high spatial frequency limit because that limit introduces an inverse length scale that is larger than the scattering coefficient.

We remark here that this derivation of the first-order scattering approximation actually does not require that $\mu_a \ll \mu_s$. We have discussed this particular case, since it connects with what has been done in SFDI using the diffusion approximation. In fact, the key balance required here is that $\mu_s \ll f_x$. Thus, the result describing the high spatial frequency behavior governed by first-order scattering applies also when there is substantial absorption in the medium.

One can develop a rigorous perturbation analysis for this problem through the scaling: $\tilde{z} = f_x z$. The asymptotic expansion of the solution will then be a power series of the form,

$$I \sim \sum_{n=0}^{\infty} \left(\frac{\mu_s}{f_x}\right)^n I_n, \quad \frac{\mu_s}{f_x} \ll 1. \quad (9)$$

The form of this power series indicates that small values of the nondimensional parameter μ_s / f_x correspond to small values of the "effective optical thickness" discussed by Chang and Ishimaru [21]. More specifically, when probing a system with a high spatial frequency, i.e., $f_x \gg \mu_s$, we are effectively interrogating a small optical thickness.

3. RADIANCE EXITING THE HALF-SPACE

Evaluating Eq. (8) on $z = 0^+$ (just inside the medium in the backward hemisphere), we find that

$$\begin{aligned} &I(\mu, \varphi, 0^+) \sim \frac{\mu_s}{2\pi f_x} \\ &\frac{\mu_0 p(\mu, \mu_0, \varphi)}{\alpha(\mu_0 - \mu) + i\left(\mu_0 \sqrt{1 - \mu^2} \cos \varphi - \mu \sqrt{1 - \mu_0^2}\right)}, \\ &-1 \leq \mu < 0, \quad 0 \leq \varphi \leq 2\pi. \end{aligned} \quad (10)$$

This leading behavior is proportional to the phase function evaluated over the backscattered hemisphere with incident direction μ_0 . For an index-matched boundary, Eq. (10) also is the radiance just outside the medium. For an index-mismatched medium, one needs to apply Snell's law and the Fresnel transmission coefficient to obtain the radiance just outside the medium. We discuss these details in Section 4.D.

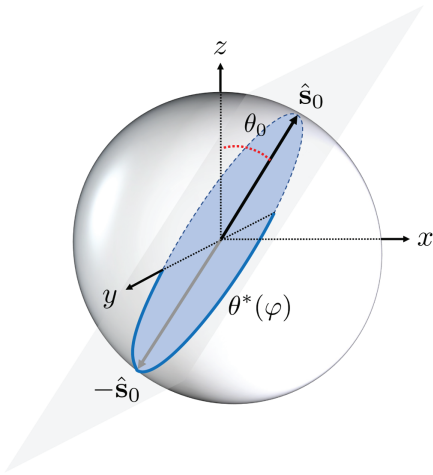


Fig. 1. Sketch of the curve $\theta^*(\varphi)$ given in Eq. (12) (solid, dark-blue curve). For $\hat{s}_0 = \sin \theta_0 \hat{x} + \cos \theta_0 \hat{z}$, the curve $\theta^*(\varphi)$ for $\pi/2 \leq \varphi \leq 3\pi/2$ follows along the portion of the great circle on the backscattered hemisphere that lies on the plane, $x \cos \theta_0 - z \sin \theta_0 = 0$, and contains the direction vectors $\pm \hat{y}$ and $-\hat{s}_0$.

Inspecting Eq. (10) and assuming that the phase function p does not vary rapidly, we observe that the radiance achieves its peak values when the absolute value of the denominator is smallest. This, in turn, happens when the imaginary part of the denominator is smallest. In fact, the imaginary part of this leading behavior can be made to be identically zero when

$$\tan \theta \cos \varphi = \tan \theta_0. \tag{11}$$

Here, $0 \leq \theta_0 < \pi/2$, $\pi/2 < \theta \leq \pi$, and $0 \leq \varphi \leq 2\pi$. Equation (11) is the intersection of the plane $x \cos \theta_0 - z \sin \theta_0 = 0$ with the unit sphere. It follows that Eq. (11) is satisfied on the curve

$$\theta^*(\varphi) = \pi + \tan^{-1} \left(\frac{\tan \theta_0}{\cos \varphi} \right), \quad \pi/2 \leq \varphi \leq 3\pi/2. \tag{12}$$

Equation (12) gives an explicit curve parameterized by the azimuthal angle $\pi/2 \leq \varphi \leq 3\pi/2$ on the backward hemisphere where the backscattered radiance is peaked. A sketch of this curve is shown in Fig. 1. For $\hat{s}_0 = \sin \theta_0 \hat{x} + \cos \theta_0 \hat{z}$, the curve $\theta^*(\varphi)$ follows along the portion of the great circle that intersects with the plane $x \cos \theta_0 - z \sin \theta_0 = 0$. Let $\hat{s}^*(\varphi)$ for $\pi/2 \leq \varphi \leq 3\pi/2$ denote the direction vector that traces this curve. As φ increases from $\varphi = \pi/2$ to π , this direction vector goes from $\hat{s}^*(\pi/2) = \hat{y}$ to $\hat{s}^*(\pi) = -\hat{s}_0$, and as φ increases from π to $3\pi/2$, this direction vector goes from $\hat{s}^*(\pi) = -\hat{s}_0$ to $\hat{s}^*(3\pi/2) = -\hat{y}$.

In Fig. 2, we plot several curves for

$$\mu^*(\varphi) = \cos \theta^*(\varphi) = - \left[1 + \left(\frac{\tan \theta_0}{\cos \varphi} \right)^2 \right]^{-1/2} \tag{13}$$

for different values of $\mu_0 = \cos \theta_0$. Depending on the value of μ_0 , we find that these curves cover different ranges of the backscattering hemisphere. When $\mu_0 = 1$ (normal incidence), it only corresponds to $\mu^* = -1$. When $\mu_0 < 1$, we find that these curves cover a broad range of the interval $-1 < \mu^* < 0$. In general, when $\mu_0 < 1$, μ^* varies across the

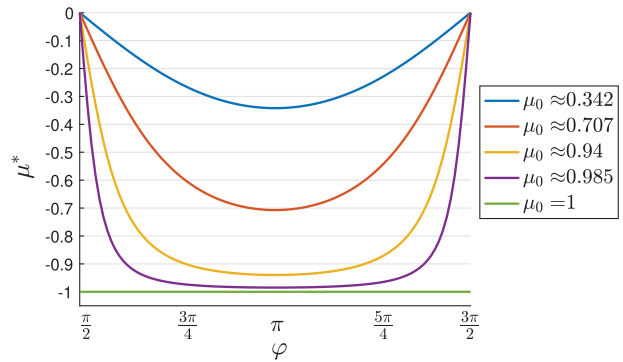


Fig. 2. Plots of the curve $\mu^*(\varphi)$ given in Eq. (9) for $\pi/2 \leq \varphi \leq 3\pi/2$ for different values of the incident direction μ_0 .

range $-\mu_0 \leq \mu^* < 0$. Therefore, with the exception of normal incidence, the larger (more grazing) the angle of incidence θ_0 , the shorter the range for μ^* .

The angular curve given in Eq. (12) depends only on the angle of incidence θ_0 , so it can be readily computed for a given experimental setup. Along this curve, Eq. (10) reduces to

$$I(\mu^*, \varphi, 0^+) \approx \frac{\mu_0 \mu_s p(\mu^*(\varphi), \mu_0, \varphi)}{\mu_a (\mu_0 - \mu^*(\varphi))}, \quad \pi/2 \leq \varphi \leq 3\pi/2. \tag{14}$$

Here, we have resubstituted $\alpha = \mu_a / (2\pi f_x)$. This leading behavior for the radiance along μ^* is purely real. Importantly, it is independent of the spatial frequency f_x . Measuring the radiance along this angular curve corresponds to sampling the scattering phase function $p(\mu^*, \mu_0, \varphi)$. Note that along this angular curve, we have $-1 \leq \cos \Theta < 0$, where $\cos \Theta = \hat{s}_0 \cdot \hat{s}^*$ is the cosine of the scattering angle. Thus, for a spherically symmetric phase function, measurement of the radiance along this curve samples the phase function over the backward hemisphere.

4. NUMERICAL RESULTS

In what follows we show results using the DOM to compute solutions of Eq. (2a) with Eq. (2b). Here we have used the Henyey–Greenstein scattering phase function,

$$p(\hat{s} \cdot \hat{s}'; g) = \frac{1}{4\pi} \frac{1 - g^2}{(1 + g^2 - 2g\hat{s} \cdot \hat{s}')^{3/2}}, \tag{15}$$

where $0 \leq g < 1$ is the anisotropy parameter. This DOM implementation uses the product quadrature rule explained in Appendix A. For the results shown here, we have used $N = 32$ to set the order of the quadrature rule, which effectively sets the truncation of the expansion of the phase function in spherical harmonics. The resulting computations give qualitatively accurate results for the distribution of the radiance over the backscattered hemisphere. The extent to which these solutions are quantitatively accurate depends strongly on the anisotropy factor. For a sharply forward-peaked scattering corresponding to $g \sim 1$, one needs a substantially higher-order computation to adequately resolve the underlying spectrum of the problem. To further verify these results, we compared them with computations using $N = 64$ and saw no appreciable difference

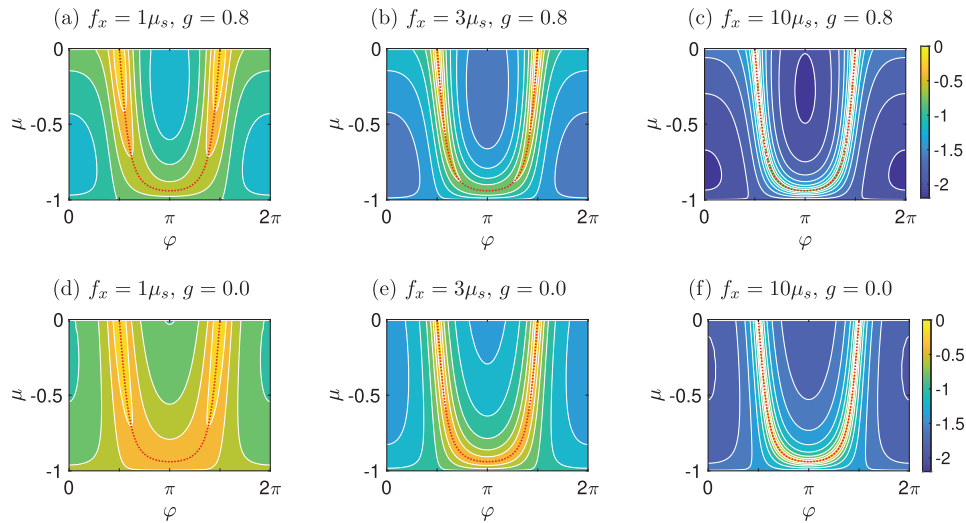


Fig. 3. Plots of the absolute value of the radiance normalized by its maximum value (\log_{10} -scale) exiting the half-space with an index-matched boundary over the backscattered hemisphere for different values of f_x and g : (a) $f_x = 1\mu_s$ and $g = 0.8$, (b) $f_x = 3\mu_s$ and $g = 0.8$, (c) $f_x = 10\mu_s$ and $g = 0.8$, (d) $f_x = 1\mu_s$ and $g = 0$, (e) $f_x = 3\mu_s$ and $g = 0$, (f) $f_x = 10\mu_s$ and $g = 0$. The dotted red curves are plots of $\mu^*(\varphi)$. Here, $\theta_0 = 20^\circ$ and $\mu_a = 0.01\mu_s$.

in the overall behavior of the radiance over the backscattered hemisphere.

The results from the DOM computation produce the radiance only over the quadrature points. To interpolate that solution over a fine mesh of 101×101 points sampling $-1 \leq \mu < 0$ and $0 \leq \varphi \leq 2\pi$, we have used the integration of source function method discussed in Appendix B. The codes used here to produce these results are available on a GitHub repository [31].

A. Index-Matched Boundary

We first consider the radiance exiting a half-space with an index-matched boundary. In Fig. 3, we show the absolute value of the radiance plotted on a \log_{10} -scale over $-1 \leq \mu < 0$ and $0 \leq \varphi \leq 2\pi$ for (a) $f_x = 1\mu_s$, (b) $3\mu_s$, and (c) $10\mu_s$. Here, the angle of incidence is $\theta_0 = 20^\circ$, and the absorption coefficient is $\mu_a = 0.01\mu_s$. The top row of plots is for anisotropy factor $g = 0.8$, and the bottom row of plots is for anisotropy factor $g = 0$.

For reference, we have plotted $\mu^*(\varphi)$ as a dotted red curve in each of the plots in Fig. 3. In these results, we observe that increases in f_x result in the increased concentration of the absolute value of the radiance concentrates along $\mu^*(\varphi)$. We find that the radiance along this curve becomes more than an order of magnitude larger as compared to distal locations on the hemisphere. Moreover, we find that the width of the concentration of radiance along this curve decreases. These results show that increases in f_x act to move the radiance distribution closer to that predicted by the first-order scattering approximation, namely, that the radiance is significantly larger along $\mu^*(\varphi)$ than elsewhere on the backscattered hemisphere. We expect some minor qualitative differences between the $g = 0.8$ and $g = 0$ results but the overall behavior to remain the same. The results shown in Fig. 3 show that this is indeed the case. Although the magnitude and width of the concentration of radiance around $\mu^*(\varphi)$ is slightly different for the two cases, we still observe the

same behavior of the onset of concentration of radiance on this curve as f_x increases.

The theory presented here indicates that the concentration of radiance about $\mu^*(\varphi)$ does not strongly depend on the optical properties, especially the phase function. The results shown in Fig. 3 confirm this.

B. Comparison with First-Order Scattering

The results from above indicate, as the theory shows, that the first-order scattering approximation becomes better as f_x increases. In Fig. 4(a), we show plots of the radiance along $\mu^*(\varphi)$ for $\pi/2 \leq \varphi \leq \pi$ (half of the curve) for different values of f_x . Here, the angle of incidence is $\theta_0 = 20^\circ$, the anisotropy factor is $g = 0$, and the absorption coefficient is $\mu_a = 0.01\mu_s$. The result from the first-order scattering approximation is plotted as a dashed black curve.

As expected, we find that the radiance along $\mu^*(\varphi)$ begins to approach the radiance given by the first-order scattering approximation evaluated on $\mu^*(\varphi)$ as f_x increases. According to Eq. (14), the radiance along $\mu^*(\varphi)$ is directly proportional to the scattering phase function. Even for moderate values of f_x , we observe that the radiance along $\mu^*(\varphi)$ exhibits the same behavior as the first-order scattering approximation.

In Fig. 4(b), we plot the first-order scattering approximation given by Eq. (14) for the radiance along μ^* for $g = 0, 0.4$, and 0.8 . These results show how g affects the behavior of the radiance along μ^* . By sampling the radiance at various points on this curve, we obtain the ability to recover quantitative information about the phase function. It is for this reason that we expect measurements along this curve to provide valuable insight into the scattering phase function of a medium.

C. Localization of the Backscattered Radiance

The results above show that the backscattered radiance is localized along the angular curve [Eq. (12)]. In particular, the

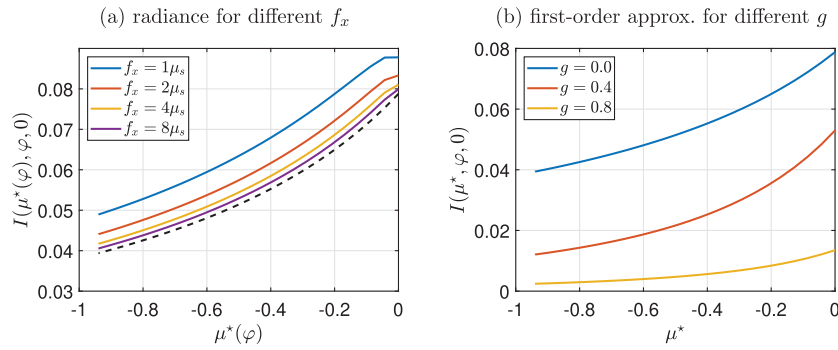


Fig. 4. (a) Comparison of the radiance along $\mu^*(\varphi)$ for $\pi/2 \leq \varphi \leq \pi$ with the first-order scattering approximation for various values of f_x with $\theta_0 = 20^\circ$, $g = 0$, and $\mu_a = 0.01\mu_s$. (b) First-order scattering approximation for the radiance on μ^* with $\theta_0 = 20^\circ$, $\mu_a = 0.01\mu_s$, and different values of the anisotropy factor.

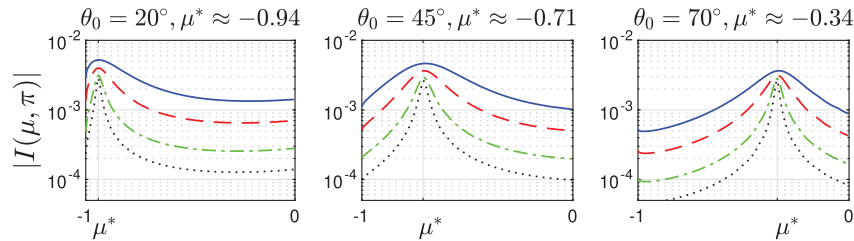


Fig. 5. Plots of the backscattered radiance (log₁₀ axis) exiting the half-space along the azimuth $\varphi = \pi$ with an index-matched boundary for a medium with $g = 0.8$, $\mu_a = 0.01\mu_s$ for the four spatial frequencies: $f_x = \mu_a$ (solid blue), $f_x = 2\mu_a$ (red dashes), $f_x = 5\mu_a$ (dot-dashes, green), and $f_x = 10\mu_a$ (black dots). The incident angles and corresponding μ^* are provided over each plot.

radiance appears to be narrow in the direction normal to this curve. In light of this, we study how the width of the radiance near the curve scales with the frequency f_x . Figure 5 shows the radiance on $\varphi = \pi$ as a function of μ (which is always normal to μ^*), i.e., $|I(\mu, \pi)|$, for a given incident angle and for several f_x values. These plots show qualitatively that the radiance attains its maximum on μ^* , and its width about this maximum decreases as the spatial frequency increases.

In addition, Fig. 6 shows the widths of the radiance near the angular curve, which are recovered as the full width at half-maximum (FWHM) of $|I|$ along the azimuth $\varphi = \pi$. The best power-law fits to the recovered widths are also plotted. Those show that the width of the angular curve decreases approximately as μ_a/f_x . Moreover, this scaling occurs across the range of the incident angles. These results can be understood from the first-order scattering approximation, (10), as $\alpha \propto \mu_a/f_x$.

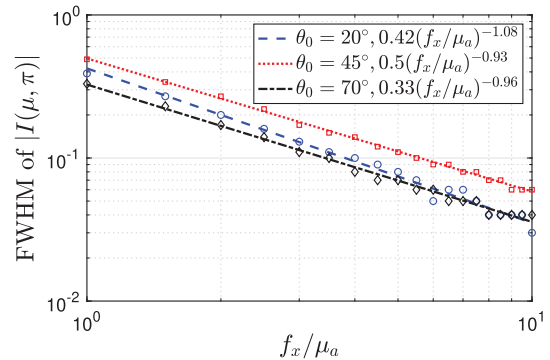


Fig. 6. FWHM of $|I(\mu, \pi)|$ (log – log axes) for spatial frequencies in the range $1 \leq f_x/\mu_a \leq 10$, for the three incident angles specified in the legend. The legend also provides the best power law fits.

denoting the refracted directions, and

$$T(\mu_{\text{out}}) = \frac{\mu_{\text{out}}}{2n^3\mu} \left[\left(\frac{2n\mu}{\mu + n\mu_{\text{out}}} \right)^2 + \left(\frac{2n\mu}{n\mu + \mu_{\text{out}}} \right)^2 \right] \quad (18)$$

denoting the Fresnel transmission coefficient for unpolarized light. Using Eq. (17), we find that

$$\mu_{\text{out}}^*(\varphi) = -\cos \left[\sin^{-1} \left(n\sqrt{1 - \mu^{*2}(\varphi)} \right) \right], \quad -1 \leq \mu^* < -\mu_c \quad (19)$$

is the refraction of $\mu^*(\varphi)$ on the backscattered hemisphere exiting the medium. This result can also be expressed as

D. Index-Mismatched Boundary

The radiance I_T exiting the medium across an index-mismatched boundary with relative refractive index $n > 1$ is given by

$$I_T(\mu_{\text{out}}, \varphi, 0) = T(\mu_{\text{out}})I(\mu, \varphi, 0), \quad (16)$$

with

$$\mu_{\text{out}} = -\cos \left[\sin^{-1} \left(n\sqrt{1 - \mu^2} \right) \right], \quad -1 \leq \mu < -\mu_c = -\sqrt{1 - n^{-2}} \quad (17)$$

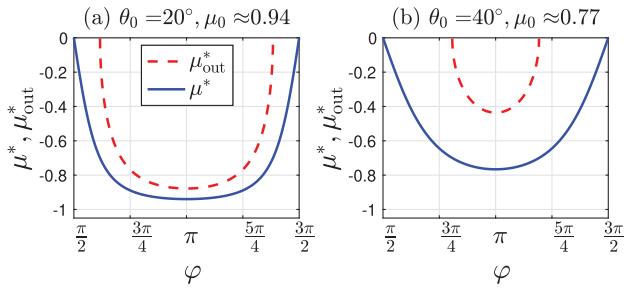


Fig. 7. Plots of $\mu^*(\varphi)$ (solid, blue) and the corresponding refracted angular curve, μ_{out}^* (red dashes), for a medium with a relative refractive index $n = 1.4$ for two incident angles. (a) $\theta_0 = 20^\circ$ ($\mu_0 \approx 0.94$); (b) $\theta_0 = 40^\circ$ ($\mu_0 \approx 0.75$).

$$\begin{aligned} \mu_{\text{out}}^*(\varphi) &= -\sqrt{1 - \frac{n^2}{1 + \frac{\cos^2 \varphi}{\tan^2 \theta_0}}}, \quad |\varphi - \pi| < \varphi_c \\ &= \cos^{-1} \left(\sqrt{n^2 - 1} \tan \theta_0 \right). \end{aligned} \quad (20)$$

Note that the backscattered radiation is negligible when the incident angle is greater than the critical angle for total internal reflection,

$$\theta_c = \cos^{-1}(\mu_c) = \sin^{-1}(1/n). \quad (21)$$

When $\theta_0 > \theta_c$, to leading order all the radiation gets trapped inside the medium.

Figure 7 shows μ^* and the corresponding refracted angular curve, μ_{out}^* as a function of $\pi/2 \leq \varphi \leq 3\pi/2$, for a medium with a relative refractive index $n = 1.4$ ($\theta_c \approx 45.5^\circ$) for two incident directions, $\theta_0 = 20^\circ$ and 40° . Compared with an index-matched boundary, the refracted angular curve has a narrower range of latitudes.

In Fig. 8, we show results of the absolute value of the radiance in a \log_{10} -scale exiting a half-space across an index-mismatched boundary for different spatial frequencies. The relative refractive index is $n = 1.4$. Additionally, we have set $\theta_0 = 20^\circ$, $g = 0.8$, and $\mu_a = 0.01\mu_s$. For reference, we have plotted μ_{out}^* as a dotted red curve in these plots.

These plots show the effect of transmitting across an index-mismatched boundary. Although the concentration of radiance along $\mu_{\text{out}}^*(\varphi)$ is wider in comparison to the index-matched results shown in Fig. 3, we see that relative magnitude of the radiance in a neighborhood about μ_{out}^* is uniformly much larger along the whole length of μ_{out}^* . This difference in relative

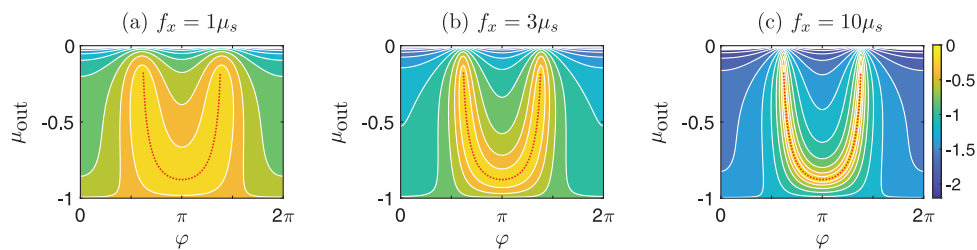


Fig. 8. Plots of the radiance normalized by its maximum value (\log_{10} axis) exiting the half-space with an index-mismatched boundary over the backscattered hemisphere for different values of f_x : (a) $f_x = 1\mu_s$, (b) $f_x = 3\mu_s$, and (c) $f_x = 10\mu_s$. The dotted red curves are plots of $\mu_{\text{out}}^*(\varphi)$. Here, $\theta_0 = 20^\circ$, $g = 0.8$, and $\mu_a = 0.01\mu_s$. The relative refractive index is $n = 1.4$.

magnitude is due to the Fresnel transmission coefficient given in Eq. (18). Nonetheless, we observe the same overall behavior of the radiance here as with the index-matched case—the concentration of radiance tends to tighten around μ_{out}^* as f_x increases.

5. CONCLUSIONS

We have studied radiative transfer in the spatial frequency domain. When the spatial frequencies are much larger than the scattering coefficient, we have shown that the leading behavior of the radiance backscattered by a medium is governed by the first-order scattering approximation. Upon studying the first-order scattering approximation, we have found a curve on the backscattered hemisphere, which we have denoted by $\mu^*(\varphi)$, on which the radiance is concentrated for large spatial frequencies. These results are inherent in radiative transfer and do not directly depend on specific optical properties of the medium.

Our numerical results confirm this theory. They show that as spatial frequency increases beyond the scattering coefficient, the radiance exiting the medium concentrates along μ^* . The radiance magnitude along μ^* increases as compared to regions away from μ^* , and the “width” of the radiance about μ^* is proportional to μ_a/f_x .

When considering the radiance exiting the medium across an index-mismatched boundary, we find that this radiance is concentrated about the mapping due to refraction of μ^* to μ_{out}^* by Snell’s law. Although the width of the resulting exiting radiance appears to be wider than that for an index-matched medium, the relative magnitude across the length of μ_{out}^* is more uniform due to the Fresnel transmission coefficient.

The first-order scattering approximation provides valuable insight into the radiance backscattered by a medium at large spatial frequencies. Specifically, we find that the radiance is directly proportional to the scattering phase function. This theoretical result supports earlier studies that sought to determine quantitative information about the scattering phase function from large spatial frequency measurements. Additionally, we have shown that the radiance along μ^* provides direct access to the scattering phase function.

These theoretical results suggest opportunities for novel measurements of backscattering by a multiple scattering medium. To the extent that one can measure the radiance on or near μ^* , one may potentially maximize information content in measurements over a narrow dynamic range. Doing so may have direct use in maximizing signal over noise, for example. Knowing that these measurements are directly proportional to the phase

function also opens up opportunities for recovering related quantitative information from these measurements.

APPENDIX A: DOM WITH PRODUCT QUADRATURE RULE

To solve Eq. (2a) subject to Eq. (2b), we write $I = I_0 + I_d$ with

$$I_0 = \delta(\mu - \mu_0)\delta(\varphi) \exp\left(-\mu_t z/\mu - i2\pi f_x \sqrt{1 - \mu^2} \cos \varphi z/\mu\right), \quad (\text{A1})$$

where $\mu_t = \mu_d + \mu_s$, and I_d satisfying

$$\begin{aligned} & \mu \partial_z I_d + i2\pi f_x \sqrt{1 - \mu^2} \cos \varphi I_d + \mu_t I_d \\ &= \mu_s \int_{-\pi}^{\pi} \int_{-1}^1 p(\mu, \mu', \varphi - \varphi') I_d(\mu', \varphi', z) d\mu' d\varphi' \\ &+ \mu_s p(\mu, \mu_0, \varphi) \exp\left(-\mu_t z/\mu_0 - i2\pi f_x \sqrt{1 - \mu_0^2} z/\mu_0\right), \end{aligned} \quad (\text{A2})$$

subject to the boundary condition

$$I_d(\mu, \varphi, 0) = r_F(\mu) I_d(-\mu, \varphi, 0) \quad \text{on } 0 < \mu \leq 1 \text{ and } -\pi \leq \varphi \leq \pi. \quad (\text{A3})$$

Here,

$$r_F(\mu) = \begin{cases} \frac{1}{2} \left(\frac{n\mu - \tilde{\mu}}{n\mu + \tilde{\mu}} \right)^2 + \frac{1}{2} \left(\frac{n\tilde{\mu} - \mu}{n\tilde{\mu} + \mu} \right)^2 & \mu_c < \mu \leq 1, \\ 1 & 0 < \mu \leq \mu_c \end{cases} \quad (\text{A4})$$

is the Fresnel reflection coefficient taking into account reflections by the refractive index mismatch on the boundary with $\mu_c = \sqrt{1 - n^{-2}}$ and $\tilde{\mu} = (1 - n^2(1 - \mu^2))^{1/2}$.

We compute I_d using a DOM that uses a product quadrature rule for Henyey–Greenstein scattering. It is well known that the Henyey–Greenstein scattering law [Eq. (15)] has the following expansion in spherical harmonics:

$$\frac{1}{4\pi} \frac{1 - g^2}{(1 + g^2 - 2g\hat{\mathbf{s}} \cdot \hat{\mathbf{s}}')^{3/2}} = \sum_{n=0}^{\infty} g^n \sum_{m=-n}^n Y_{nm}(\hat{\mathbf{s}}) Y_{nm}^*(\hat{\mathbf{s}}'). \quad (\text{A5})$$

It follows that for any sufficiently smooth function $\psi(\hat{\mathbf{s}})$,

$$\begin{aligned} J[\psi](\hat{\mathbf{s}}) &= \int_{4\pi} \frac{1}{4\pi} \frac{1 - g^2}{(1 + g^2 - 2g\hat{\mathbf{s}} \cdot \hat{\mathbf{s}}')^{3/2}} \psi(\hat{\mathbf{s}}') d\hat{\mathbf{s}}' \\ &= \sum_{n=0}^{\infty} g^n \sum_{m=-n}^n Y_{nm}(\hat{\mathbf{s}}) \int_{4\pi} Y_{nm}^*(\hat{\mathbf{s}}') \psi(\hat{\mathbf{s}}') d\hat{\mathbf{s}}'. \end{aligned} \quad (\text{A6})$$

By truncating this series beyond the first N terms, we introduce the following approximation:

$$\mathcal{J}[\psi](\hat{\mathbf{s}}) \approx \mathcal{J}^N[\psi](\hat{\mathbf{s}}) = \sum_{n=0}^N g^n \sum_{m=-n}^n Y_{nm}(\hat{\mathbf{s}}) \int_{4\pi} Y_{nm}^*(\hat{\mathbf{s}}') \psi(\hat{\mathbf{s}}') d\hat{\mathbf{s}}'. \quad (\text{A7})$$

We compute the integral in the expression above using the product Gauss quadrature rule [32], which takes the form

$$\int_{4\pi} Y_{nm}^*(\hat{\mathbf{s}}') \psi(\hat{\mathbf{s}}') d\hat{\mathbf{s}}' \approx \frac{\pi}{N} \sum_{j=1}^{2N} \sum_{i=1}^N w_i Y_{nm}^*(\mu_i, \varphi_j) \psi(\mu_i, \varphi_j), \quad (\text{A8})$$

with μ_i and w_i for $i = 1, \dots, N$ denoting the N -point Gauss–Legendre quadrature points and weights, respectively, and $\varphi_j = (j - 1)\pi/N$ for $j = 1, \dots, 2N$.

The sums in Eq. (A8) can be written as a matrix-vector product, where the vector has entries corresponding to $\psi(\mu_i, \varphi_j)$ for $i = 1, \dots, N$ and $j = 1, \dots, 2N$. It follows that the evaluation of Eq. (A7) with the integral replaced by Eq. (A8) and evaluated on these quadrature points is a matrix-vector product. A MATLAB code that implements this method and produces this matrix is available for download [31]. Let J^N denote this matrix. By evaluating Eq. (A2) on these quadrature points, we obtain the following system of linear ordinary differential equations:

$$\begin{aligned} A \partial_z \mathbf{I}_d(z) + i2\pi f_x B \mathbf{I}_d(z) + \mu_t \mathbf{I}_d(z) &= \mu_s J^N \mathbf{I}_d(z) \\ &+ \mathbf{f}(z) \exp\left(-\mu_t z/\mu_0 - i2\pi f_x \sqrt{1 - \mu_0^2} z/\mu_0\right). \end{aligned} \quad (\text{A9})$$

Here, $\mathbf{I}_d(z)$ corresponds to evaluating I_d on the quadrature points. The diagonal matrix A corresponds to evaluating μ on the quadrature points, the diagonal matrix B corresponds to evaluating $\sqrt{1 - \mu^2} \cos \varphi$ on the quadrature points, and $\mathbf{f}(z)$ corresponds to evaluating $\mu_s p(\mu, \mu_0, \varphi)$ on the quadrature points. Additionally, we evaluate Eq. (A3) on the quadrature points and obtain

$$\Lambda_+ \mathbf{I}_d(0) = R_F \Lambda_- \mathbf{I}_d(0). \quad (\text{A10})$$

Here, Λ_{\pm} restricts the entries of \mathbf{I}_d to $\mu \geq 0$, respectively, and R_F is a diagonal matrix corresponding to the evaluation of $r_F(\mu)$ on the quadrature points for $\mu > 0$.

Using numerical linear algebra methods, one can compute the exact solution of Eq. (A9) with Eq. (A10). The result will be $\mathbf{I}_d(z)$, which gives the radiance on the quadrature points.

APPENDIX B: INTEGRATION OF SOURCE FUNCTION INTERPOLATION METHOD

Let us rewrite Eq. (A2) as

$$\mu \partial_z I_d + \left(\mu_t + i2\pi f_x \sqrt{1 - \mu^2} \cos \varphi \right) I_d = \mu_s S_1 + \mu_s S_2, \quad (\text{B1})$$

with

$$S_1(\mu, \varphi, z) = \int_{-\pi}^{\pi} \int_{-1}^1 p(\mu, \mu', \varphi - \varphi') I(\mu', \varphi', z) d\mu' d\varphi', \quad (\text{B2})$$

and

$$\begin{aligned} S_2(\mu, \varphi, z) &= p(\mu, \mu_0, \varphi) \\ &\times \exp\left(-\mu_t z/\mu_0 - i2\pi f_x \sqrt{1 - \mu_0^2} z/\mu_0\right). \end{aligned} \quad (\text{B3})$$

Suppose we have used the DOM to solve the RTE, yielding $\mathbf{I}_d(\mathbf{z})$, whose entries correspond to

$$[\mathbf{I}_d(\mathbf{z})]_{ij} \approx I(\mu_i, \varphi_j, \mathbf{z}), \quad i = 1, \dots, N, \quad j = 1, \dots, 2N, \quad (\text{B4})$$

with μ_i for $i = 1, \dots, N$ denoting the N -point Gauss–Legendre quadrature points and $\varphi_j = (j - 1)\pi/N$ for $j = 1, \dots, 2N$. Let

$$S_1^N(\mu, \varphi, \mathbf{z}) = \frac{\pi}{M} \sum_{j=1}^{2N} \sum_{i=1}^N w_i p(\mu, \mu_i, \varphi - \varphi_j) [\mathbf{I}_d(\mathbf{z})]_{ij}. \quad (\text{B5})$$

Using S_1^N , we compute the approximation,

$$I_d(\mu, \varphi, 0) \approx \frac{\mu_s}{\mu} \int_0^\infty e^{(\mu_i + i2\pi f_x \sqrt{1-\mu^2} \cos \varphi)z'/\mu} \times [S_1^N(\mu, \varphi, z') + S_2(\mu, \varphi, z')] dz', \quad (\text{B6})$$

on $-1 \leq \mu < 0$ and $-\pi \leq \varphi \leq \pi$. Integration in the expression above can be performed analytically. This result can then be used to interpolate the solution over the backscattered hemisphere. This integration of source function interpolation method has been established as the most accurate method for interpolating the radiance [33].

Funding. Air Force Office of Scientific Research (FA9550-21-1-0196); National Science Foundation (DMS-1840265, MRI-1429783).

Acknowledgment. A. D. Kim is supported by the AFOSR and the NSF. Part of this research was conducted using the MERCED cluster funded by the NSF at the Cyberinfrastructure and Research Technologies (CIRT) at UC Merced.

Disclosures. The authors declare no conflicts of interest.

Data availability. Data underlying the results presented in this paper are not publicly available at this time but may be obtained from the authors upon reasonable request.

REFERENCES

- D. J. Cuccia, F. Bevilacqua, A. J. Durkin, and B. J. Tromberg, "Modulated imaging: quantitative analysis and tomography of turbid media in the spatial-frequency domain," *Opt. Lett.* **30**, 1354–1356 (2005).
- D. J. Cuccia, F. P. Bevilacqua, A. J. Durkin, F. R. Ayers, and B. J. Tromberg, "Quantitation and mapping of tissue optical properties using modulated imaging," *J. Biomed. Opt.* **14**, 024012 (2009).
- J. Angelo, S. Chen, M. Ochoa, U. Sunar, S. Gioux, and X. Intes, "Review of structured light in diffuse optical imaging," *J. Biomed. Opt.* **24**, 071602 (2018).
- S. Nothelfer, F. Bergmann, A. Liemert, D. Reitzle, and A. Kienle, "Spatial frequency domain imaging using an analytical model for separation of surface and volume scattering," *J. Biomed. Opt.* **24**, 071604 (2018).
- C. K. Hayakawa, K. Karrobi, V. E. Pera, D. M. Roblyer, and V. Venugopalan, "Optical sampling depth in the spatial frequency domain," *J. Biomed. Opt.* **24**, 071603 (2018).
- S. C. Kanick, D. M. McClatchy, V. Krishnaswamy, J. T. Elliott, K. D. Paulsen, and B. W. Pogue, "Sub-diffusive scattering parameter maps recovered using wide-field high-frequency structured light imaging," *Biomed. Opt. Express* **5**, 3376–3390 (2014).
- D. M. McClatchy, E. J. Rizzo, W. A. Wells, P. P. Cheney, J. C. Hwang, K. D. Paulsen, B. W. Pogue, and S. C. Kanick, "Wide-field quantitative imaging of tissue microstructure using sub-diffuse spatial frequency domain imaging," *Optica* **3**, 613–621 (2016).
- J. R. Mourant, J. Boyer, A. H. Hielscher, and I. J. Bigio, "Influence of the scattering phase function on light transport measurements in turbid media performed with small source–detector separations," *Opt. Lett.* **21**, 546–548 (1996).
- A. Kienle, F. K. Forster, and R. Hibst, "Influence of the phase function on determination of the optical properties of biological tissue by spatially resolved reflectance," *Opt. Lett.* **26**, 1571–1573 (2001).
- F. Bevilacqua and C. Depeursinge, "Monte Carlo study of diffuse reflectance at source–detector separations close to one transport mean free path," *J. Opt. Soc. Am. A* **16**, 2935–2945 (1999).
- A. Pardo, S. S. Streeter, B. W. Maloney, J. A. Gutiérrez-Gutiérrez, D. M. McClatchy, W. A. Wells, K. D. Paulsen, J. M. López-Higuera, B. W. Pogue, and O. M. Conde, "Modeling and synthesis of breast cancer optical property signatures with generative models," *IEEE Trans. Med. Imaging* **40**, 1687–1701 (2021).
- F. Foschum and A. Kienle, "Optimized goniometer for determination of the scattering phase function of suspended particles: simulations and measurements," *J. Biomed. Opt.* **18**, 085002 (2013).
- A. Wax, C. Yang, V. Backman, M. Kalashnikov, R. R. Dasari, and M. S. Feld, "Determination of particle size by using the angular distribution of backscattered light as measured with low-coherence interferometry," *J. Opt. Soc. Am. A* **19**, 737–744 (2002).
- J. W. Pyhtila and A. Wax, "Rapid, depth-resolved light scattering measurements using Fourier domain, angle-resolved low coherence interferometry," *Opt. Express* **12**, 6178–6183 (2004).
- A. Wax, C. Yang, V. Backman, K. Badizadegan, C. W. Boone, R. R. Dasari, and M. S. Feld, "Cellular organization and substructure measured using angle-resolved low-coherence interferometry," *Biophys. J.* **82**, 2256–2264 (2002).
- D. W. Shipp, R. Qian, and A. J. Berger, "Angular-domain scattering interferometry," *Opt. Lett.* **38**, 4750–4753 (2013).
- G. Rybicki, "The searchlight problem with isotropic scattering," *J. Quant. Spectrosc. Radiat. Transfer* **11**, 827–849 (1971).
- C. Siewert and W. Dunn, "The searchlight problem in radiative transfer," *J. Quant. Spectrosc. Radiat. Transfer* **41**, 467–481 (1989).
- L. Barichello and C. Siewert, "The searchlight problem for radiative transfer in a finite slab," *J. Comput. Phys.* **157**, 707–726 (2000).
- M. Williams, "The searchlight problem in radiative transfer with internal reflection," *J. Phys. A: Math. Theor.* **40**, 6407 (2007).
- H.-W. Chang and A. Ishimaru, "Beam wave propagation and scattering in random media based on the radiative transfer theory," *J. Wave-Mater. Interact.* **2**, 41–69 (1987).
- A. D. Kim and M. Moscoso, "Radiative transfer computations for optical beams," *J. Comput. Phys.* **185**, 50–60 (2003).
- A. D. Kim and M. Moscoso, "Beam propagation in sharply peaked forward scattering media," *J. Opt. Soc. Am. A* **21**, 797–803 (2004).
- M. Machida, G. Y. Panasyuk, J. C. Schotland, and V. A. Markel, "The Green's function for the radiative transport equation in the slab geometry," *J. Phys. A: Math. Theor.* **43**, 065402 (2010).
- M. Machida, "Numerical algorithms of the radiative transport equation using rotated reference frames for optical tomography with structured illumination," *J. Quant. Spectrosc. Radiat. Transfer* **234**, 124–138 (2019).
- A. R. Gardner, A. D. Kim, and V. Venugopalan, "Radiative transport produced by oblique illumination of turbid media with collimated beams," *Phys. Rev. E* **87**, 063308 (2013).
- S. Gioux, A. Mazhar, and D. J. Cuccia, "Spatial frequency domain imaging in 2019: principles, applications, and perspectives," *J. Biomed. Opt.* **24**, 071613 (2019).
- A. Ishimaru, *Wave Propagation and Scattering in Random Media* (IEEE, 1997).
- M. Ramírez-Cabrera, C. Arancibia-Bulnes, and P. Valades-Pelayo, "The first-order scattering approximation: a closed-form extension to Beer's law, accurate for weakly scattering media," *J. Quant. Spectrosc. Radiat. Transfer* **262**, 107412 (2021).
- L. Florescu, J. C. Schotland, and V. A. Markel, "Single-scattering optical tomography," *Phys. Rev. E* **79**, 036607 (2009).
- A. D. Kim, "SFD-radiativetransfer," Github (2022), <https://github.com/arnolddkim/SFD-RadiativeTransfer>.
- K. E. Atkinson, "Numerical integration on the sphere," *ANZIAM J.* **23**, 332–347 (1982).
- A. H. Karp, "Computing the angular dependence of the radiation of a planetary atmosphere," *J. Quant. Spectrosc. Radiat. Transfer* **25**, 403–412 (1981).